

Dark-bright solitons in coupled NLS equations with unequal dispersion coefficients

E. G. Charalampidis

*School of Civil Engineering, Faculty of Engineering,
Aristotle University of Thessaloniki,
Thessaloniki 54124, Greece*
and

Department of Mathematics and Statistics, University of Massachusetts, Amherst, MA 01003-4515, USA

P. G. Kevrekidis

Department of Mathematics and Statistics, University of Massachusetts, Amherst, MA 01003-4515, USA

D. J. Frantzeskakis

Department of Physics, University of Athens, Panepistimiopolis, Zografos, Athens 15784, Greece

B. A. Malomed

*Department of Physical Electronics, School of Electrical Engineering,
Faculty of Engineering, Tel Aviv University, Tel Aviv 69978, Israel*

(Dated: December 6, 2024)

We study a two-component nonlinear Schrödinger system with repulsive nonlinear interactions and different dispersion coefficients in the two components. We consider states that have a dark solitary wave in the one-component. Treating it as a “frozen” one, we explore the possibility of the formation of bright solitonic bound states in the other component. We identify bifurcation points of such states in the linear limit for the bright component, and explore their continuation in the nonlinear regime. An additional analytically tractable limit is found to be that of vanishing dispersion of the bright component. We numerically identify regimes of potential stability not only of the single-peak ground state (the dark-bright solitary wave), but also of excited states with one or more zero crossings in the bright component. When the states are identified as unstable, direct numerical simulations are used to investigate the outcome of the instability manifestation.

I. INTRODUCTION

Atomic Bose-Einstein condensates (BECs) [1, 2] constitute a platform which is ideal for the study of numerous nonlinear wave phenomena; see, e.g., the recent reviews [3–6]. One of the particularly interesting directions in that regard, has been the study of multi-component BEC systems and solitary waves therein. This is a subject of broad interest, not only in the realm of atomic BECs, but also in nonlinear optics [7], as well as in studies of integrable systems in mathematical physics [8]. Arguably, one of the most intriguing coherent structures in the multi-component settings under the presence of defocusing nonlinearities (in terms of optical systems), or repulsive inter-atomic interactions (in BECs), are the dark-bright (DB) solitons. In particular, exact solutions for such states are available in the well-known integrable self-defocusing two-component Manakov system [9]. Generally, the DB solitons are ubiquitous in two-component systems, i.e. the nonlinear Schrödinger or Gross-Pitaevskii equations (NLSE or GPE), in which both the self- and cross-phase modulations (SPM and XPM) are represented by cubic terms.

In the DB structures, the customary dark soliton of the defocusing NLSE induces an effective potential, via the XPM interaction, in the other component, which, in turn, produces self-trapping of bright-soliton states in the latter component. This possibility has been studied extensively in atomic BECs; see, e.g., Refs. [10–19]. Such waveforms have been reported in experiments, both in two-component BEC mixtures, which make use of two different atomic states of ^{87}Rb [20–25], and in nonlinear optics [26–28]. The BEC experimental studies have examined the dynamics of a single DB soliton in a trap [20, 22], the generation of multiple DB solitons in a counterflow experiment [21], the study of their interactions [23], as well as the creation of $SU(2)$ -rotated DB solitons, in the form of beating dark-dark solitons [24, 25].

Our aim in the present work is to attempt to carry this fundamental structural idea for the existence of DB solitary waves a bit further, i.e., beyond the integrable or very close to integrable limit of the Manakov model. In fact, the nearly-integrable setting has been especially useful and relevant to the experiment, due to the fact that the ratios of inter- and intra-species interactions between different hyperfine atomic states of ^{87}Rb in the BEC mixtures ($|1, 0\rangle$ and $|2, 0\rangle$, as well as $|1, -1\rangle$ and $|2, -2\rangle$) are very close to unity. The “dispersion” coefficients in this setting are equal too, as they are determined by the same atomic weight. It is relevant to note in passing that, quite recently [29], the studies of spin-orbit-coupled BECs [30] have lead to a set of coupled GPEs (via a multiple-scale reduction scheme) where the effective dispersion coefficients could differ substantially (and controllably), as they depend on the curvature of the

corresponding dispersion relation of the two-component branches.

The possibility of having different dispersion prefactors (which are also different, e.g., for the system of coupled GPEs corresponding to a BEC mixture with different atomic masses) in the model producing the DB solitary waves, provides our main motivation for the present work. In particular, if we assume the dark soliton to be a(n approximately) “frozen” potential imposed by, say, the first component to the second (bright) one, then varying the dispersion coefficient allows to modulate the effective depth and width of the “effective potential”. In so doing, we can trap different numbers of bound states, at the level of the linear approximation for the bright component. Our theoretical analysis presented in Section II, allows us then to infer the dispersion –and eigenvalue, so-called chemical potential– parameters for which multiple such states would become accessible. Another intriguing limit is the limit of vanishing dispersion of the second component. Given the algebraic nature of the second equation in that limit, we can treat that limit analytically as well and test our solutions therein (this is also presented in section II). Based on these theoretical aspects of the analysis (the linear and algebraic nonlinear limits), we then numerically examine the bifurcation of nonlinear solutions from the predicted linear theory bifurcation points and their potential continuation (when possible all the way to the zero-dispersion limit). Not only do we identify these solutions, but we explore their spectral characteristics, finding, as may be natural to expect, the waveforms to be more prone to instability, the higher the excited state i.e., the more nodes the bright structure possesses. When unstable, we numerically explore the solutions’ dynamical features involving often mobility of the coherent structure, but also in the case of higher excited states the potential for destruction or reshaping into a lower excited state. This computational analysis is performed in section III. Finally, in section IV, we summarize our findings and present our conclusions, as well as highlight some directions for future study.

II. THE MODEL AND ANALYTICAL CONSIDERATIONS

Given that the underlying model is relevant to both atomic BECs and nonlinear optics, we present it in the general form of the coupled NLS equations. Although we do not include a trapping potential (which may be particularly relevant in the case of BEC [3]), we focus on the existence of modes supported only by the nonlinear interactions. It is natural to expect that the solutions presented below would be, generally, more robust if the trapping potential is additionally included; i.e., the analysis in the free space is thus the most challenging issue.

Here, we consider the coupled NLS system (in the absence of an external potential) written in the following dimensionless form

$$i\partial_t\Phi_- = -\frac{D_-}{2}\partial_{xx}\Phi_- + \gamma(g_{11}|\Phi_-|^2 + g_{12}|\Phi_+|^2)\Phi_-, \quad (1a)$$

$$i\partial_t\Phi_+ = -\frac{D_+}{2}\partial_{xx}\Phi_+ + \gamma(g_{21}|\Phi_-|^2 + g_{22}|\Phi_+|^2)\Phi_+, \quad (1b)$$

with dispersion coefficients D_\pm , nonlinearity constant γ and interaction coefficients g_{jk} ($j, k = 1, 2$ and $g_{21} \equiv g_{12}$). In BECs of different species, D_\pm play the role of the inverse masses, while in the spin-orbit BECs application of [29], they are associated with the local curvature of the different branches of the dispersion relation. The fields $\Phi_\pm = \Phi_\pm(x, t)$ in Eqs. (1) will correspond to the dark (with “–” sign) and bright (with “+” sign) -soliton components, respectively. We fix $g_{jk} = 1$ for all $j, k = 1, 2$ (motivated by the actual situation for the BEC mixtures in ^{87}Rb) and $D_- = \gamma = 1$ (which is always possible upon rescaling), while we set $D_+ \equiv D (\geq 0)$. Stationary solutions of Eqs. (1) can be found using the ansatz $\Phi_\pm(x, t) = \phi_\pm(x) \exp(-i\mu_\pm t)$, where $\phi_\pm(x)$ are real-valued functions, and μ_\pm are the effective chemical potentials. Then, Eqs. (1) reduce to the coupled system of stationary equations

$$\mu_- \phi_- = -\frac{1}{2}\partial_{xx}\phi_- + (\phi_-^2 + \phi_+^2)\phi_-, \quad (2a)$$

$$\mu_+ \phi_+ = -\frac{D}{2}\partial_{xx}\phi_+ + (\phi_-^2 + \phi_+^2)\phi_+. \quad (2b)$$

for the unknown steady state solutions ϕ_\pm . In the absence of the bright component, i.e. $\phi_+ = 0$, an obvious dark-soliton solution is given by

$$\phi_-(x) = \sqrt{\mu_-} \tanh(\sqrt{\mu_-}x). \quad (3)$$

With this solution playing the role of the background for the small bright component ϕ_+ , the linearized form of equation (2b) in the field ϕ_+ for given μ_- leads to an eigenvalue problem in the form of

$$\mathcal{L}\phi_+ = \lambda\phi_+, \quad (4)$$

where $\mathcal{L} = \frac{D}{2}\partial_{xx} + \mu_- \text{sech}^2(\sqrt{\mu_-}x)$ is a linear operator, and (λ, ϕ_+) is the eigenvalue-eigenvector pair with $\lambda \equiv \mu_- - \mu_+$. According to standard results from quantum mechanics [37] for this well-known Pöschl-Teller potential [31], Eq. (4) gives rise to the bound state of order n ($n = 0$ corresponds to the ground spatially even state, $n = 1$ to the first odd state, etc.) which exists under the following condition

$$D < D_{\text{crit}}^{(n)} = 2/[n(1+n)]. \quad (5)$$

In particular, the ground state is always present, while the first odd state exists at $D < 1$, the first excited even state ($n = 2$) exists at $D < 1/3$, the next excited odd state ($n = 3$) exists at $D < 1/6$ and so on.

It can thus be expected that nonlinear solutions corresponding to the ground and excited states of the linear limit will bifurcate at these critical values of D with the corresponding eigenvalues μ_+ of the linear problem (4); on the other hand, μ_- is a given amplitude of the background for the dark soliton which is set to unity in our numerical computations below.

As explained in the Introduction, $D = 0$ is an additional limit of the problem that can be treated analytically. In that case, Eqs. (2a) and (2b) degenerate into

$$\frac{1}{2}\phi_-'' + (\mu_- - \mu_+)\phi_- = 0, \quad \phi_+^2(x) = \mu_+ - \phi_-^2(x), \quad \text{at } \phi_-^2 < \mu_+, \quad (6a)$$

$$\mu_- \phi_- = -\frac{1}{2}\phi_-'' + \phi_-^3, \quad \phi_+ = 0, \quad \text{at } \phi_-^2 > \mu_+. \quad (6b)$$

This is a case reminiscent of the well-known Thomas-Fermi approximation [1–3] for ϕ_- in the context of atomic BECs, with the difference that the role of the potential here is played by the component ϕ_+ . Solutions to Eqs. (6a) and (6b) exist for $\mu_- > \mu_+$, like in the case of Eq. (4). Odd solutions are built as

$$\begin{aligned} \phi_-(x) &= \phi_0 \sin\left(\sqrt{2(\mu_- - \mu_+)}x\right), \quad \phi_+^2(x) = \mu_+ - \phi_-^2(x), \quad \text{at } |x| < \xi, \\ \phi_-(x) &= \text{sgn}(x)\sqrt{\mu_-} \tanh\left(\sqrt{\mu_-}(|x| - x_0)\right), \quad \phi_+ = 0, \quad \text{at } |x| > \xi. \end{aligned} \quad (7)$$

where constants ϕ_0 , ξ , and x_0 are determined by the three matching conditions,

$$\begin{aligned} \phi_0 \sin\left(\sqrt{2(\mu_- - \mu_+)}\xi\right) &= \sqrt{\mu_+}, \\ \sqrt{\mu_-} \tanh\left(\sqrt{\mu_-}(\xi - x_0)\right) &= \sqrt{\mu_+}, \\ \phi_0 \sqrt{2(\mu_- - \mu_+)} \cos\left(\sqrt{2(\mu_- - \mu_+)}\xi\right) &= \frac{\mu_-}{\cosh^2\left(\sqrt{\mu_-}(\xi - x_0)\right)}. \end{aligned} \quad (8)$$

An exact analytical solution of Eq. (8) can be found in the form

$$\begin{aligned} \phi_0 &= \sqrt{\frac{1}{2}(\mu_- + \mu_+)}, \\ \xi - x_0 &= (1/\sqrt{\mu_-}) \tanh^{-1}\left(\sqrt{\frac{\mu_+}{\mu_-}}\right), \\ \xi &= \frac{1}{\sqrt{2(\mu_- - \mu_+)}} \left[\sin^{-1}\left(\sqrt{\frac{2\mu_+}{\mu_- + \mu_+}}\right) + 2\pi n \right], \end{aligned} \quad (9)$$

where $n = 0$ represents the single DB soliton, while higher values of n correspond to a larger number of DBs, e.g., $n = 1$ corresponds to 5 etc. It is clear that via this approach exact analytical formulas can be derived for the various branches of solutions for $D = 0$ (although, given the cumbersome nature of the formulas, we will not discuss such higher order analytical forms here).

III. THE COMPUTATIONAL ANALYSIS

A. Numerical Methods

Throughout this section, numerical results are presented for the coupled NLS system (1). Our investigation addresses three basic issues: *existence*, *stability* and *dynamical evolution*. The first two are considered by performing one-parameter continuation of the steady-state solution, varying the chemical potential μ_+ , for different values of the

dispersion coefficient D . When the solutions are found to be unstable/stable, their dynamical evolution is monitored by means of direct numerical simulations to explore/corroborate the outcome of the instability/stability.

Initially, we employ a one-dimensional uniform spatial grid consisting of N points labeled by $x_j = -L + 2jL/(N+1)$ and $j = 1, \dots, N$ with lattice spacing (resolution) δx and half-width L . The left and right boundary points are located at $j = 0$ and $j = N+1$, respectively. In all the cases studied herein we fix $\delta x = 0.1$ and $L = 30$ (except for the evolution of the first excited symmetric state with $D = 0.25$ and $\mu_+ = 0.99$, where we use $L = 60$). This way, both fields $\phi_{\pm}(x)$ and $\Phi_{\pm}(x, t)$ are replaced by their discrete counterparts on the spatial grid, i.e. $\phi_{j,\pm} = \phi_{\pm}(x_j)$ and $\Phi_{j,\pm}(t) = \Phi_{\pm}(x_j, t)$, respectively. Then, the second-order spatial derivatives in Eqs. (1) and (2) (as well as in Eqs. (A3a) and (A3e) in the Appendix A) are replaced by second-order central-difference formulas. Finally, the no-flux boundary conditions are applied at the edges of the spatial grid, i.e. $\partial_x \phi_{\pm}|_{x=\pm L} = 0$ and $\partial_x \Phi_{\pm}(t)|_{x=\pm L} = 0$, for all t . The latter are coupled into the internal discretization scheme using first-order forward and backward difference formulas at the left and right boundaries, respectively. Thus, the no-flux boundary conditions are enforced by explicitly requiring $\phi_{0,\pm} = \phi_{1,\pm}$ and $\phi_{N+1,\pm} = \phi_{N,\pm}$, as well as $\Phi_{0,\pm}(t) = \Phi_{1,\pm}(t)$ and $\Phi_{N+1,\pm}(t) = \Phi_{N,\pm}(t)$.

As far as the existence part is concerned, steady-state solutions of Eqs. (2) are identified by employing a Newton-Krylov method [38], together with a suitable initial guess in order to ensure convergence. To that end, our starting point is the eigenvalue problem (4) which is solved numerically. In particular, we focus on a bound state of order n and we pick a value of D satisfying the threshold condition (5). Then, we determine the value of μ_+ corresponding to one of the lowest eigenvalues λ (although the choice made here is adjusted appropriately to the particular bound state studied) and the corresponding eigenvector (or bright component) ϕ_+ is obtained afterwards. As a result, the “seed” fed into our nonlinear solver consists, essentially, of the pair (μ_+, ϕ_+) together with the dark component ϕ_- given by Eq. (3). Next, we trace steady-state solutions, for a given value of dispersion coefficient D , by performing a single-parameter numerical continuation, with chemical potential μ_+ to be the continuation parameter. Our approach is based on the *sequential continuation* method, i.e., providing the solution for given μ_+ found by the nonlinear solver, as the “seed” for the next continuation step. We corroborate our results using the *pseudo-arclength continuation* method (see, for instance, [39] and references therein), although numerical results using the sequential method are reported throughout this section.

Furthermore, we investigate the stability of the steady states obtained by our Newton solvers at each continuation step, using linearized equations for small perturbations (see Appendix A). In particular, an eigenvalue problem (cf. Eq. (A2)) is obtained (at order $\mathcal{O}(\varepsilon)$) and solved numerically afterwards. The steady state is classified as a stable one if none of the eigenfrequencies $\omega = \omega_r + i\omega_i$ has a non-vanishing imaginary part ω_i . If the steady state possesses at least one eigenfrequency with $\omega_i \neq 0$, this signals the presence of an instability. Two types of instabilities can be thus identified: i) *exponential instabilities* characterized by a pair of eigenfrequencies with *zero* real part, and ii) *oscillatory instabilities* characterized by a complex eigenfrequency quartet.

Finally, the spectral stability results obtained from the eigenvalue problem are checked against direct dynamical evolution of the coupled NLS system (1) forward in time. To this end, the Dormand and Prince method (DOP853) with an automatic time-step adaption procedure (see, the appendix in [40]) and tolerance 10^{-13} is employed. We have also corroborated our results using the standard fourth-order Runge-Kutta method (RK4) with a fixed time-step of $\delta t = 10^{-4}$, although numerical results are presented throughout this section using only the DOP853 method. Thus, we initialize the dynamics at $t = 0$ using the steady states obtained, although two distinct initialization approaches can be discerned. On the one hand, we initialize the dynamics under the presence of a small (uniformly distributed) random perturbation with amplitude 10^{-3} for the class of stable steady states studied herein. An alternative approach utilized is to initialize the dynamics using the linearization ansatz given by Eqs. (A1) for the unstable solutions with $\varepsilon = 10^{-2}$ (except for the first excited antisymmetric steady state with $D = 0.2$ and $\mu_+ = 0.77$, while $\varepsilon = 10^{-1}$) where we pick the eigenvector V corresponding to the (complex) eigenfrequency having a maximal imaginary part. The latter approach is useful towards seeding the relevant instability and observing the ensuing dynamics.

B. Numerical Results

In this subsection, numerical results are presented for the coupled NLS system (1) and organized following the reasoning mentioned in the previous subsection. First, Figs. 1-2 and 4-5 summarize the results on the existence of steady-state solutions and the corresponding parametric continuations (using μ_+ as the continuation parameter, at different fixed values of D) for bound states of order $n = 0$ (ground states with a single-hump bright component, corresponding to a generalization of the DB solitary waves), $n = 1$ (the first excited odd states), $n = 2$ (the second excited states, which are spatially even), and $n = 3$ (the third excited states overall, and second excited odd ones), respectively. Specifically, panels (a) illustrate examples of dark and bright soliton solutions (black and blue solid lines, respectively) which, according to our stability analysis, are stable (see panels (c) in Figs. 6-9 below). Next, panels (b) complement the existence results and present stability characteristics, namely, the dominant unstable eigenfrequency.

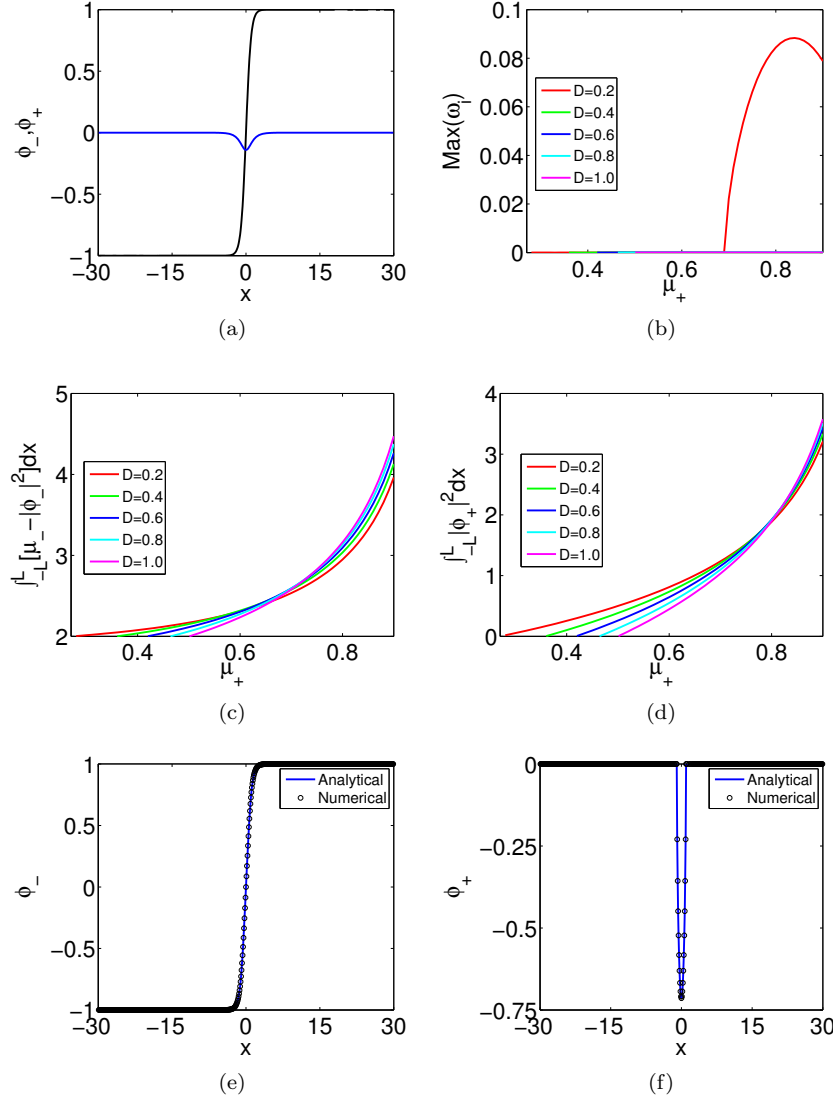


FIG. 1: (Color online) Bound states and continuation results corresponding to $n = 0$ (i.e. ground states). *Top row*: Steady state profiles (a) of the dark (black line) and bright (blue line) soliton solutions for values of the parameters of $D = 1$ and $\mu_+ = 0.51$. Maximal imaginary eigenfrequency (b) as a function of the continuation parameter μ_+ and for various fixed values of D . *Middle row*: Solution measures, i.e., the power associated with the solution branches, namely $\int_{-L}^L [\mu_- - |\phi_-|^2] dx$ (c) and $\int_{-L}^L |\phi_+|^2 dx$ (d), respectively, both as functions of the continuation parameter μ_+ and for various (fixed) values of D . *Bottom row*: Dark (e) and bright (f) soliton solutions analytically predicted (7) (blue line) and numerically obtained (black circles) for $D = 0$ and $\mu_+ = 0.51$.

Furthermore, panels (c) and (d) summarize our existence results by presenting $\int_{-L}^L [\mu_- - |\phi_-|^2] dx$ and $\int_{-L}^L |\phi_+|^2 dx$, respectively, as functions of μ_+ and for various fixed values of D . These integrals correspond to the total power in optics or the atom number in the atomic BEC, considered as a function of the propagation constant or chemical potential, respectively.

In particular, it can be inferred from Fig. 1(b) that solutions corresponding to the ground state are stable for values of $D = 0.4$ through $D = 1.0$ and for all values of μ_+ within the range of interest. On the contrary, the solution branch corresponding to $D = 0.2$ is stable till a critical point $\mu_+^{\text{crit}} \approx 0.69$, while past this value an exponential instability, in terms of an imaginary eigenfrequency pair with zero real part, emerges (see also Fig. 6(f)). Similar arguments can be applied to panels (b) of Figs. 2, 4 and 5, although the description is somewhat different. In particular, it can be discerned in Fig. 2(b) that the solution branch corresponding to $D = 0.2$ possesses a number of instability intervals for $\mu_+ > 0.71$. However, in the present case the instability manifests itself by a complex eigenfrequency quartet, i.e., an oscillatory instability corresponding to a Hamiltonian Hopf bifurcation (see also Fig. 7(i) below as a case example); for a recent discussion of relevant bifurcations, see e.g. [41]. While instabilities of this type are present as shown

in Fig. 3(a), past the value of $\mu_+ \approx 0.8252$ an additional imaginary eigenfrequency pair appears too, as depicted in Fig. 3(b) and is initially marked with a red dashed-dotted line in Fig. 2(b). As μ_+ further increases, the exponentially unstable mode grows (cf. Fig. 3(c)) and becomes dominant (cf. Fig. 3(d)), while the oscillatory one follows a smaller growth rate, as depicted in Fig. 2(b) with a red dash-dotted line (the crossing of the solid with the dash-dotted line marks the exchange of the dominant form of instability). This is also the case for the solution branches with $D = 0.4$ and $D = 0.6$ depicted in Fig. 2(b) with green and blue dashed-dotted lines, respectively. This transition effect between the exponentially and oscillatorily unstable modes also arises for the bound states of order $n = 2$ (cf. Fig. 4(b)) and $n = 3$, (cf. Fig. 5(b)). An additional feature that arises in the latter figures is well-known in the context of discrete systems as a finite-size effect, and it was introduced in [42] (see also [43]). This involves the fact that the continuous spectrum of background (phonon) excitations is “discretized” on our spatial grid, hence complex eigenfrequencies may return to the real eigenfrequency axis temporarily before colliding with another pair to exit again as quartets. It is expected (cf. Refs. [42] and [43]) that these discrete effects gradually disappear as the spectrum becomes more dense, i.e., in the infinite-domain limit. It is the combination of the above-mentioned exchanges of the dominant instability type and of the temporary restabilizations that gives rise to the spikes in panels (b) in Figs. 4 and 5. In such cases, only the dominant instability growth rate is shown; recall that Fig. 4 presents the results for the second excited (first excited even) branch, and Fig. 5 those for the third excited (second excited odd) branch.

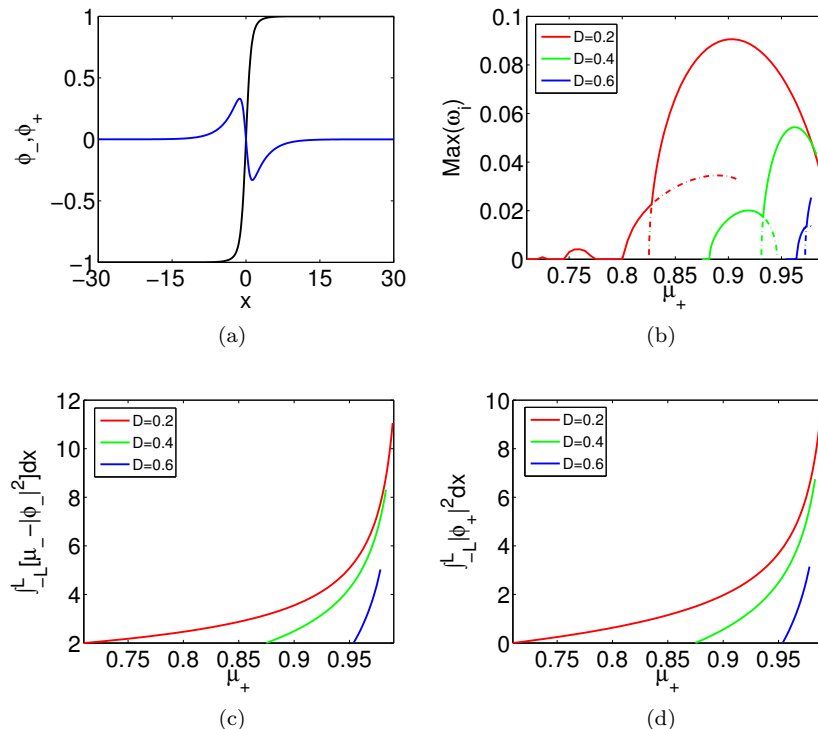


FIG. 2: (Color online) Same as Fig. 1 but for bound states of order $n = 1$ (i.e. first excited spatially odd states). *Top row*: Steady state profiles (a) of the dark (black line) and bright (blue line) soliton solutions for values of the parameters of $D = 0.6$ and $\mu_+ = 0.96$. Maximal imaginary eigenfrequency (b) as a function of the continuation parameter μ_+ and for various (fixed) values of D . Notice that the second highest instability growth rates are also shown with dash-dotted lines (see text, for details). *Bottom row*: Solution branch measures, i.e., the power associated with the solution branches, namely $\int_{-L}^L [\mu_- - |\phi_-|^2] dx$ (c) and $\int_{-L}^L |\phi_+|^2 dx$ (d), respectively, both as functions of the continuation parameter μ_+ and for various (again, fixed) values of D .

As a general comment, it is worthwhile to note that the branches with higher n are generally more prone to instability than branches with lower n . The ground state single-hump solution is generally fairly robust, as is suggested by the observability of the DB soliton in both atomic and optical settings [20–22, 26]. Our results reveal that only at very lower values of D does an instability arise for this state. On the other hand, branches with $n = 1$ to $n = 3$ are less robust. Among them, our results suggest that the $n = 1$ branch attains the highest instability growth rates. However, examining the parametric intervals of the instability (i.e., widths of the intervals of μ_+ over which the branches remain stable), we observe that the higher the n , the narrower the corresponding stability interval becomes. Nevertheless, it should be noted that the instability growth rates are relatively weak, typically $\sim 10^{-2}$, which suggests that the solutions should be long-lived ones, as the dynamical simulations which we now turn, will corroborate.

Finally, we present results on the evolution of perturbed steady-state solutions of orders $n = 0$, $n = 1$, $n = 2$ and $n = 3$ (for various values of D and μ_+) in Figs. 6-9, respectively. In particular, the first and second columns correspond to the spatio-temporal evolution of the dark and bright components, respectively, while the corresponding eigenfrequency spectra of perturbations around the steady states (for which the evolution is examined) are presented in the third columns. For the stable steady states at hand, see panels (a) in Figs. 1-2 and Figs. 4-5, the corresponding dynamical evolution of the dark (panels (a)) and bright (panels (b)) components are depicted in the top rows of Figs. 6-9, respectively. Clearly, the stable solutions are indeed persistent, in the presence of small-in-amplitude random perturbations, within the reported time range of the simulations.

On the contrary, a number of different scenarios are observed for the unstable solutions depending upon the corresponding dominant unstable eigenmode, as predicted by computations of the eigenfrequencies. Specifically, steady states perturbed along the unstable eigendirection corresponding to an exponential eigenmode typically appear lead to soliton mobility. This is the case in panels (d)-(e) of Figs. 6-8 and panels (g)-(h) of Fig. 9, where motion of the solitons is observed. While for the fundamental branch this type of the mobility may be persistent, for the higher excited states the acceleration induced by the instability eventually leads to a breakdown of the solution (an apparent “merging” of the dark-in-bright solitons therein [32]) after a sufficient amount of time has elapsed.

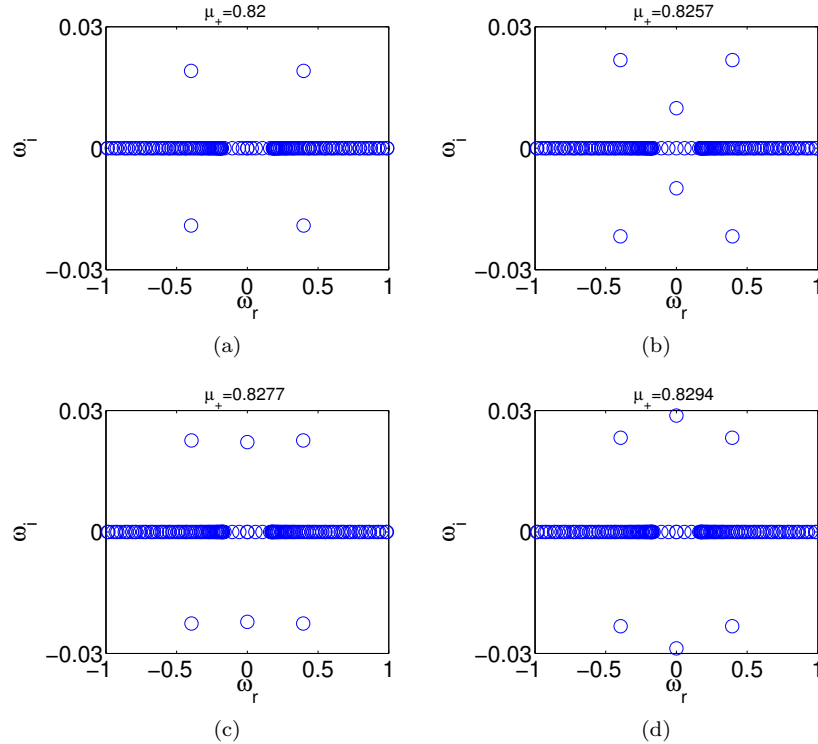


FIG. 3: (Color online) Eigenfrequency spectra corresponding to bound states of order $n = 1$ with $D = 0.2$ and for various values of μ_+ .

A number of additional possibilities appears to emerge when unstable steady states are perturbed along oscillatory eigenmodes. This leads to oscillatory growth eventually translating into an apparent “jerky” motion of the corresponding dark and bright components. This behavior is presented in Figs. 7(g)-7(h) (for $n = 1$) [here it is clear that the instability wipes out the initial dark-in-bright solitary wave, transforming the bright component into a fundamental single-peak mode]. It also appears in Figs. 8(g)-8(h) (for $n = 2$), where an explosion breaks apart the entire solitary wave. In Figs. 8(j)-8(k) (i.e. for $n = 2$), we observe a progression through the instability from a two-node solution in the bright component to a single-node state, and, eventually, to a fundamental one. Lastly, in Figs. 9(d)-9(e), a rapid destruction of the $n = 3$ state occurs again, now directly transforming it into the fundamental state. In Figs. 9(j)-9(k), a more complex scenario arises with the dark soliton splitting off into apparently gray ones, the fastest of which is not accompanied by a bright counterpart. As a result, the bright component appears to disperse, maintaining, however, some of its nodal structure. Finally, in Figs. 9(m)-9(n) (once again, for $n = 3$), the third excited state (the second spatially odd one) transforms itself into the corresponding first excited state.

It is worth noting that, for the fundamental branch, there is at most a “translational” (imaginary) eigenfrequency responsible for the instability. It is thus rather natural that its manifestation in direct simulations involves mobility. However, as we progressively move to higher excited states, the number of potentially unstable modes increases,

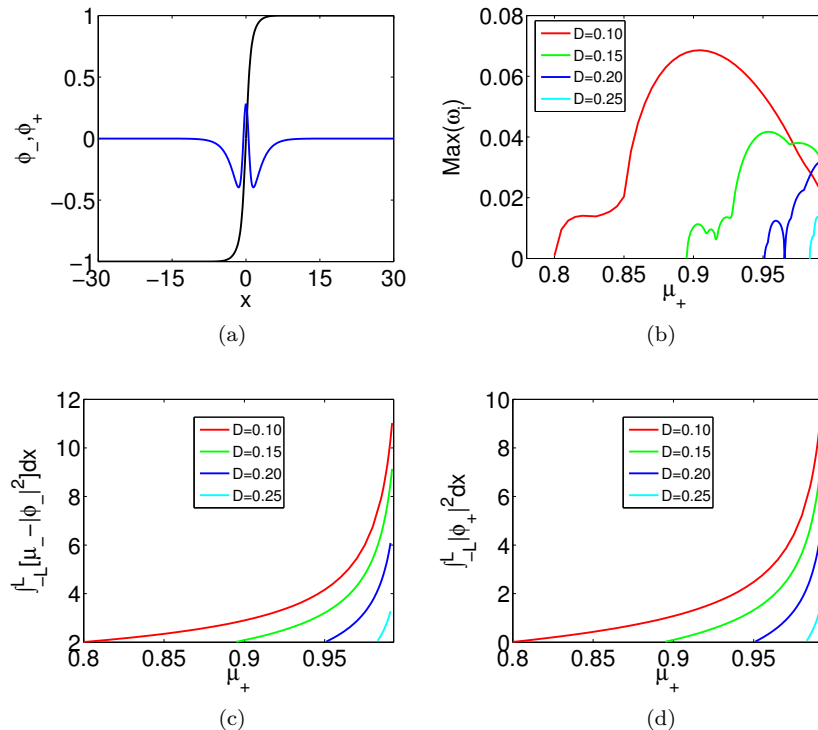


FIG. 4: (Color online) Same as Fig. 1 but for bound states of order $n = 2$ (i.e. first excited spatially even states). *Top row:* Steady state profiles (a) of the dark (black line) and bright (blue line) soliton solutions for values of the parameters of $D = 0.2$ and $\mu_+ = 0.9655$. Maximal imaginary eigenfrequency (b) as a function of the continuation parameter μ_+ and for various values of D . *Bottom row:* the power associated with the solution branches as a function of the continuation parameter μ_+ and for various values of D .

creating an oscillatory instability for $n = 1$, two for $n = 2$, and so on, as n increases, in accordance with Figs. 7, 8 etc. It is the intricate interplay of these distinct dynamical instabilities (often with comparable growth rates) that is responsible for the resulting complex dynamics.

IV. CONCLUSIONS

In the present work, we have revisited the two-component, nonlinear Schrödinger equation with the defocusing nonlinearity, which is relevant for nonlinear optics, as well as for the description of repulsively interacting binary BEC mixtures. We have re-examined the fundamental dynamical features of DB (dark-bright) solitons, namely, the formation of the effective potential well for the bright component induced by the dark one. Utilizing the dispersion coefficient of the bright component as a control parameter, we modified the depth of the effective well, enabling the formation of higher-order excited bound states within this well, including $n = 1$, $n = 2$ and $n = 3$ nodes. The latter can be thought of as states with dark-in-bright solitary structures [32], or as excited states trapped in the potential well. We saw that, while the ground single-peak state is generally very robust (except for the case of a high difference between the dispersion coefficients of the two components), this is not true for the excited states, which are subject to progressively wider intervals of both monotonously growing and oscillatory instabilities. The instability of the ground state leads to motion of the DB soliton, but does not destroy it. For the excited states with progressively increasing n , the complexity of the evolution scenarios also increases, resulting from the interplay of the increasing number of instability modes. Exotic scenarios involve the fusion of the dark-in-bright solitary waves, the explosion of the waveforms towards multiple splinters, and their transformation –either abruptly or progressively– to less excited states.

The present analysis suggests a number of paths for future studies. On the one hand, one can extend the present considerations to the quite important (e.g. in BEC) and widely studied class of spinor systems, involving more than two components [33]. Following this possibility, one can envision, in the spirit of Ref. [34], one dark component creating a potential for the other two bright components, which could find themselves either in the same or, for suitable parametric regimes, possibly in different states of their respective potential wells. This would be a particularly

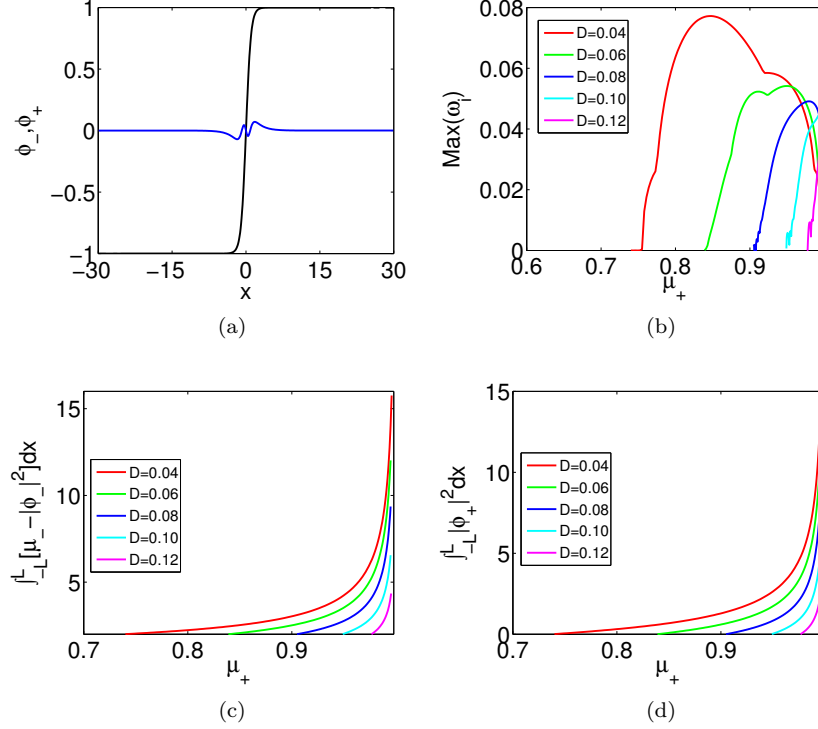


FIG. 5: (Color online) Same as Fig. 1 but for bound states of order $n = 3$ (i.e. second excited antisymmetric states). *Top row:* Steady state profiles (a) of the dark (black line) and bright (blue line) soliton solutions for values of the parameters of $D = 0.12$ and $\mu_+ = 0.977$. The rest of the panels are similar in Fig. 4.

intriguing setup to explore, both at the level of existence but also at that of stability properties. Furthermore, we note that the possibility of one component forming a well for another is independent of the spatial dimension. For instance, in two dimensions the notion of vortex-bright solitons [35, 36] is a by-product of the same type of potential approach (the topological charge of the vortices is not “felt” by the bright component, when the interaction is incoherent, i.e., the potential well is solely determined by the density distribution in the vortex). Here, it would be interesting to explore what type of excited states could be created, such as a dark-in-bright ring and associated multi-ring states, *inter alia*. Such states are currently under examination and will be presented in future publications.

Acknowledgments. E.G.C. gratefully acknowledges financial support from the FP7-People IRSES-606096: “*Topological Solitons, from Field Theory to Cosmos*”. He also thanks Hans Johnston (UMass) for providing computing facilities. The work of D.J.F. was partially supported by the Special Account for Research Grants of the University of Athens. P.G.K. acknowledges support from the National Science Foundation under grants CMMI-1000337, DMS-1312856, from FP7-People under grant IRSES-606096 and from the US-AFOSR under grant FA9550-12-10332. The work of P.G.K. and B.A.M. is supported, in a part, by the Binational (US-Israel) Science Foundation through grant 2010239.

Appendix A: The linearization ansatz and stability matrix

In this appendix, we shortly discuss the linearization ansatz employed for the investigation of the stability of the stationary solutions, together with the formulation of the stability matrix. We start with the perturbation ansatz around stationary solutions $\phi_{\pm}^0(x)$ (which may be complex, in principle)

$$\tilde{\Phi}_- = e^{-i\mu_- t} \left[\phi_-^0 + \varepsilon \left(a(x)e^{i\omega t} + b^*(x)e^{-i\omega^* t} \right) \right], \quad (\text{A1a})$$

$$\tilde{\Phi}_+ = e^{-i\mu_+ t} \left[\phi_+^0 + \varepsilon \left(c(x)e^{i\omega t} + d^*(x)e^{-i\omega^* t} \right) \right], \quad (\text{A1b})$$

where ω is the (complex) eigenfrequency and ε is a small amplitude of the perturbation, while the superscript asterisk (*) stands for the complex conjugation. Then, we insert Eqs. (A1) into Eqs. (1) and thus obtain (at order $\mathcal{O}(\varepsilon)$) an

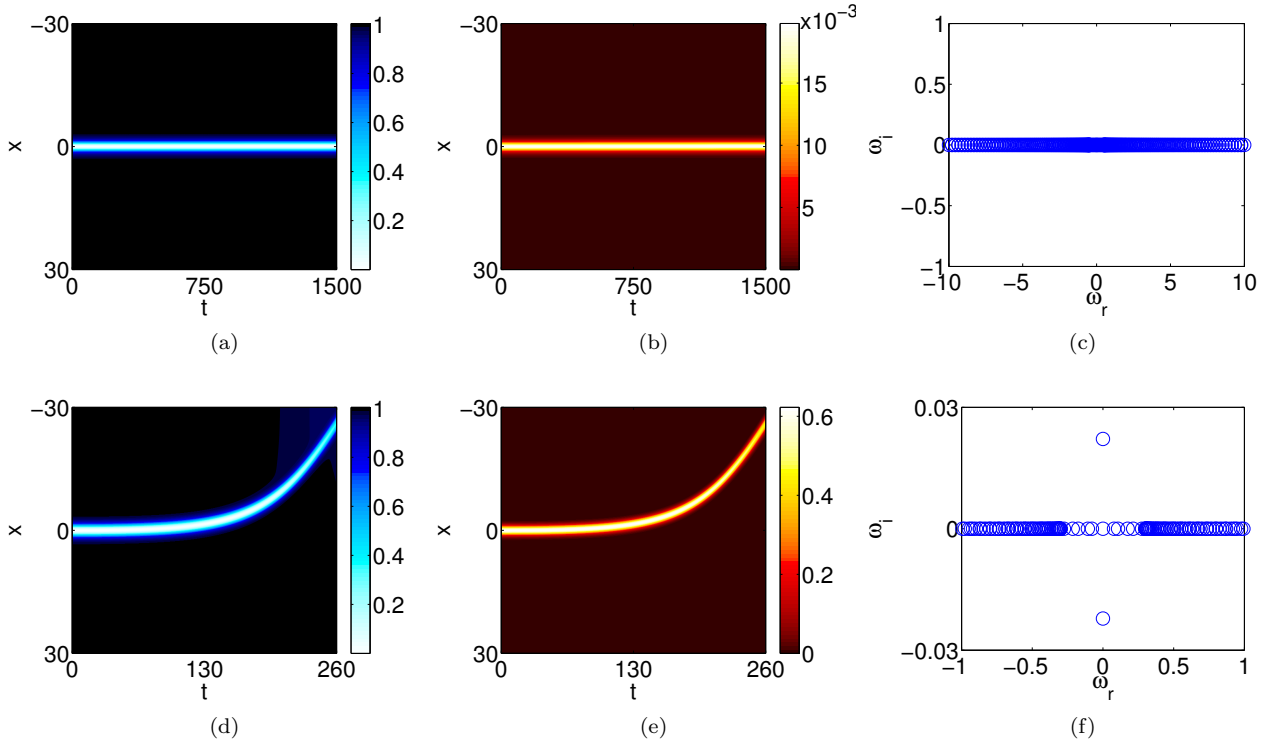


FIG. 6: (Color online) Spatio-temporal evolution of the densities $|\Phi_-(x,t)|^2$ (first column) and $|\Phi_+(x,t)|^2$ (second column) corresponding to (perturbed) soliton solutions of order $n = 0$, as well as the eigenfrequency spectrum of the identified steady states (third column). Top and bottom rows correspond to values of the parameters of $D = 1$ with $\mu_+ = 0.51$ and $D = 0.2$ with $\mu_+ = 0.7$, respectively.

eigenvalue problem in the following matrix form

$$\rho \begin{pmatrix} a \\ b \\ c \\ d \end{pmatrix} = \begin{pmatrix} A_{11} & A_{12} & A_{13} & A_{14} \\ -A_{12}^* & -A_{11} & -A_{14}^* & -A_{13}^* \\ A_{13}^* & A_{14} & A_{33} & A_{34} \\ -A_{14}^* & -A_{13} & -A_{34}^* & -A_{33} \end{pmatrix} \begin{pmatrix} a \\ b \\ c \\ d \end{pmatrix}, \quad (\text{A2})$$

with eigenvalues $\rho = -\omega$, eigenvectors $V = (a, b, c, d)^T$ and matrix elements given by

$$A_{11} = -\frac{D_-}{2} \frac{\partial^2}{\partial x^2} + \gamma (2g_{11}|\phi_-^0|^2 + g_{12}|\phi_+^0|^2) - \mu_1, \quad (\text{A3a})$$

$$A_{12} = \gamma g_{11} (\phi_-^0)^2, \quad (\text{A3b})$$

$$A_{13} = \gamma g_{12} \phi_-^0 (\phi_+^0)^*, \quad (\text{A3c})$$

$$A_{14} = \gamma g_{12} \phi_-^0 \phi_+^0, \quad (\text{A3d})$$

$$A_{33} = -\frac{D_+}{2} \frac{\partial^2}{\partial x^2} + \gamma (g_{12}|\phi_-^0|^2 + 2g_{22}|\phi_+^0|^2) - \mu_2, \quad (\text{A3e})$$

$$A_{34} = \gamma g_{22} (\phi_+^0)^2. \quad (\text{A3f})$$

-
- [1] C. J. Pethick and H. Smith, *Bose-Einstein condensation in dilute gases* (Cambridge University Press, Cambridge, 2002).
 - [2] L. P. Pitaevskii and S. Stringari, *Bose-Einstein Condensation* (Oxford University Press, Oxford, 2003).
 - [3] P. G. Kevrekidis, D. J. Frantzeskakis, and R. Carretero-González, *Emergent Nonlinear Phenomena in Bose-Einstein Condensates: Theory and Experiment* (Springer-Verlag, Heidelberg, 2008).
 - [4] R. Carretero-González, D. J. Frantzeskakis, and P. G. Kevrekidis, *Nonlinearity* **21**, R139 (2008).
 - [5] F. Kh. Abdullaev, A. Gammal, A. M. Kamchatnov, and L. Tomio, *Int. J. Mod. Phys. B* **19**, 3415 (2005).
 - [6] D. J. Frantzeskakis, *J. Phys. A: Math. Theor.* **43**, 213001 (2010).
 - [7] Yu. S. Kivshar and G. P. Agrawal, *Optical solitons: from fibers to photonic crystals*, Academic Press (San Diego, 2003).

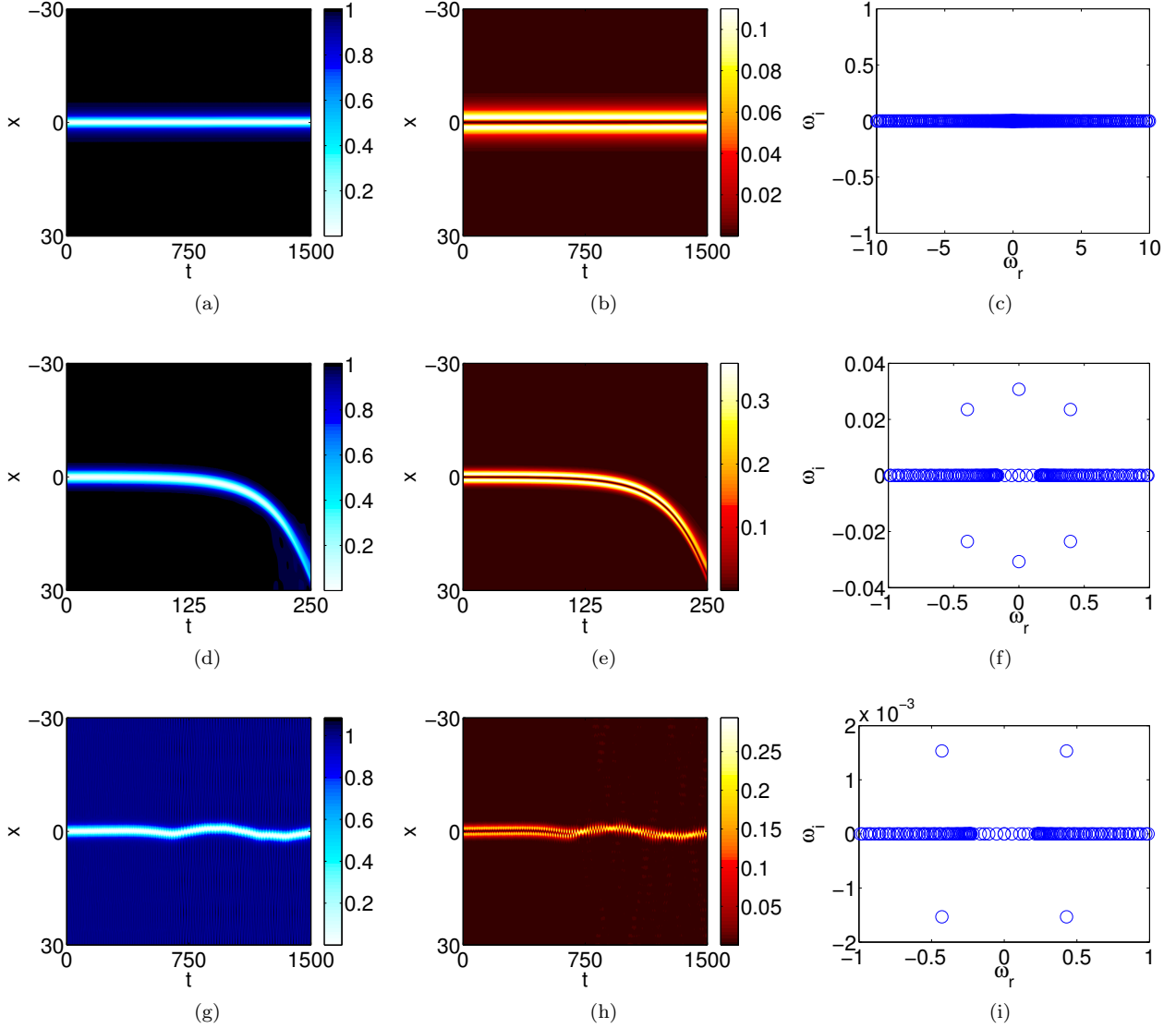


FIG. 7: (Color online) Same as Fig. 6 but for soliton solutions of order $n = 1$. First and second columns correspond to spatio-temporal evolution of the densities $|\Phi_{-}(x, t)|^2$ and $|\Phi_{+}(x, t)|^2$, respectively, whereas the third column corresponds to the eigenfrequency spectrum of the identified steady state solutions. Top row corresponds to values of the parameters of $D = 0.6$ and $\mu_{+} = 0.96$, whereas both middle and bottom rows correspond to $D = 0.2$, although with $\mu_{+} = 0.83$ (middle row) and $\mu_{+} = 0.77$ (bottom row), respectively.

- [8] M. J. Ablowitz, B. Prinari and A. D. Trubatch, *Discrete and Continuous Nonlinear Schrödinger Systems*, Cambridge University Press (Cambridge, 2004).
- [9] S. V. Manakov, Sov. Phys. JETP **38**, 248 (1974).
- [10] Th. Busch and J. R. Anglin, Phys. Rev. Lett. **87**, 010401 (2001).
- [11] H. E. Nistazakis, D. J. Frantzeskakis, P. G. Kevrekidis, B. A. Malomed, and R. Carretero-González, Phys. Rev. A **77**, 033612 (2008).
- [12] M. Vijayajayanthi, T. Kanna, and M. Lakshmanan, Phys. Rev. A **77**, 013820 (2008).
- [13] S. Rajendran, P. Muruganandam, M. Lakshmanan, J. Phys. B **42**, 145307 (2009).
- [14] V. A. Brazhnyi and V. M. Pérez-García, Chaos, Solitons & Fractals **44**, 381 (2011).
- [15] C. Yin, N. G. Berloff, V. M. Perez-Garcia, V. A. Brazhnyi, and H. Michinel, Phys. Rev. A **83**, 051605 (2011).
- [16] K. J. H. Law, P. G. Kevrekidis, and L. S. Tuckerman, Phys. Rev. Lett. **105**, 160405 (2010).
- [17] A. Álvarez, J. Cuevas, F. R. Romero, and P. G. Kevrekidis, Physica D **240**, 767 (2011).
- [18] V. Achilleos, P. G. Kevrekidis, V. M. Rothos, and D. J. Frantzeskakis, Phys. Rev. A **84**, 053626 (2011).
- [19] V. Achilleos, D. Yan, P. G. Kevrekidis, and D. J. Frantzeskakis, New J. Phys. **14**, 055006 (2012).
- [20] C. Becker, S. Stellmer, P. Soltan-Panahi, S. Dörscher, M. Baumert, E.-M. Richter, J. Kronjäger, K. Bongs, and K.

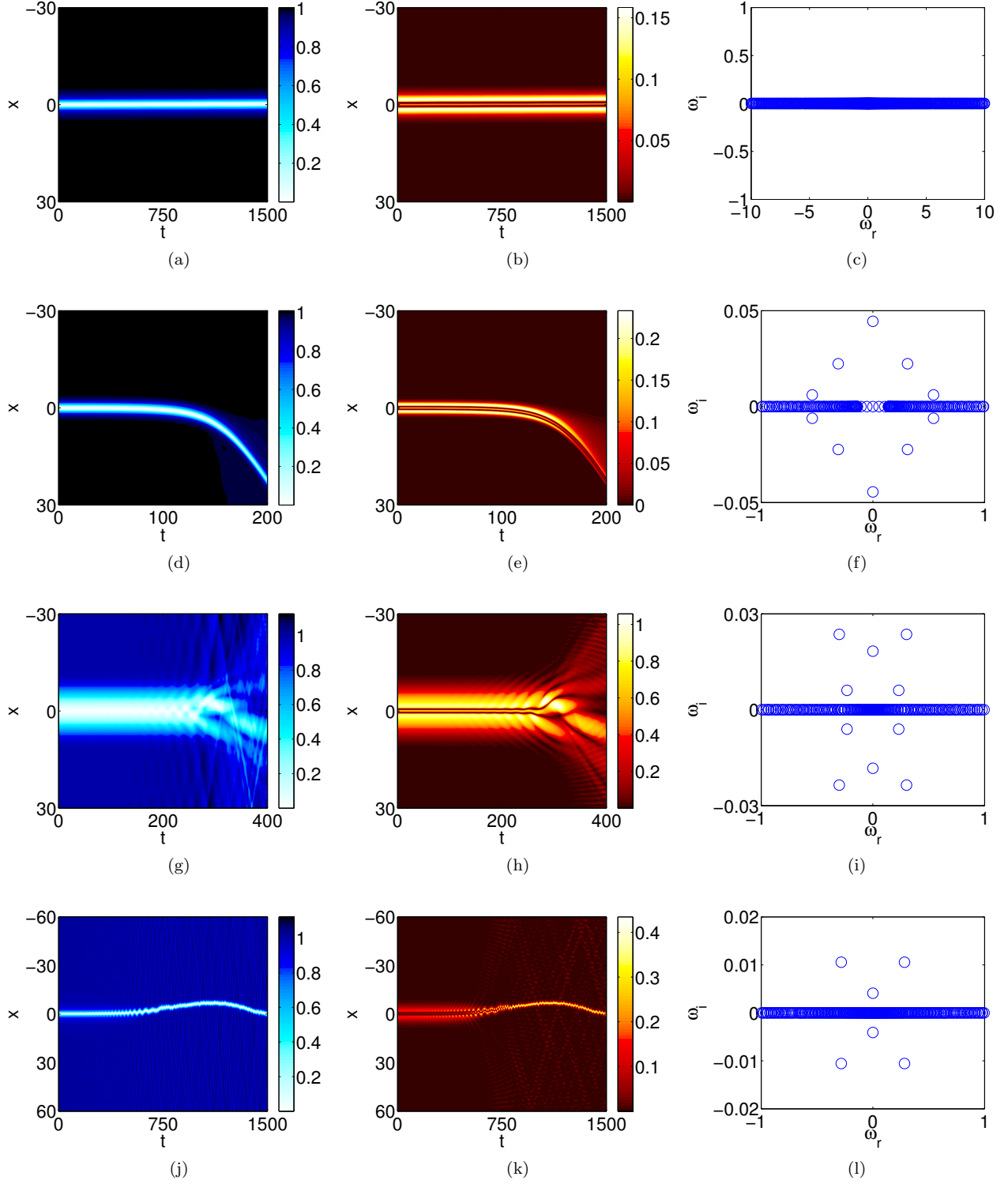


FIG. 8: (Color online) Same as Fig. 6 but for soliton solutions of order $n = 2$. First and second columns correspond to spatio-temporal evolution of the densities $|\Phi_-(x, t)|^2$ and $|\Phi_+(x, t)|^2$, respectively, whereas the third column corresponds to the eigenfrequency spectrum of the identified steady state solutions. First row corresponds to values of the parameters of $D = 0.2$ and $\mu_+ = 0.9655$, whereas both second and third rows correspond to $D = 0.1$, although with $\mu_+ = 0.86$ (second row) and $\mu_+ = 0.99$ (third row), respectively. Finally, the fourth row corresponds to values of the parameters of $D = 0.25$ and $\mu_+ = 0.99$.

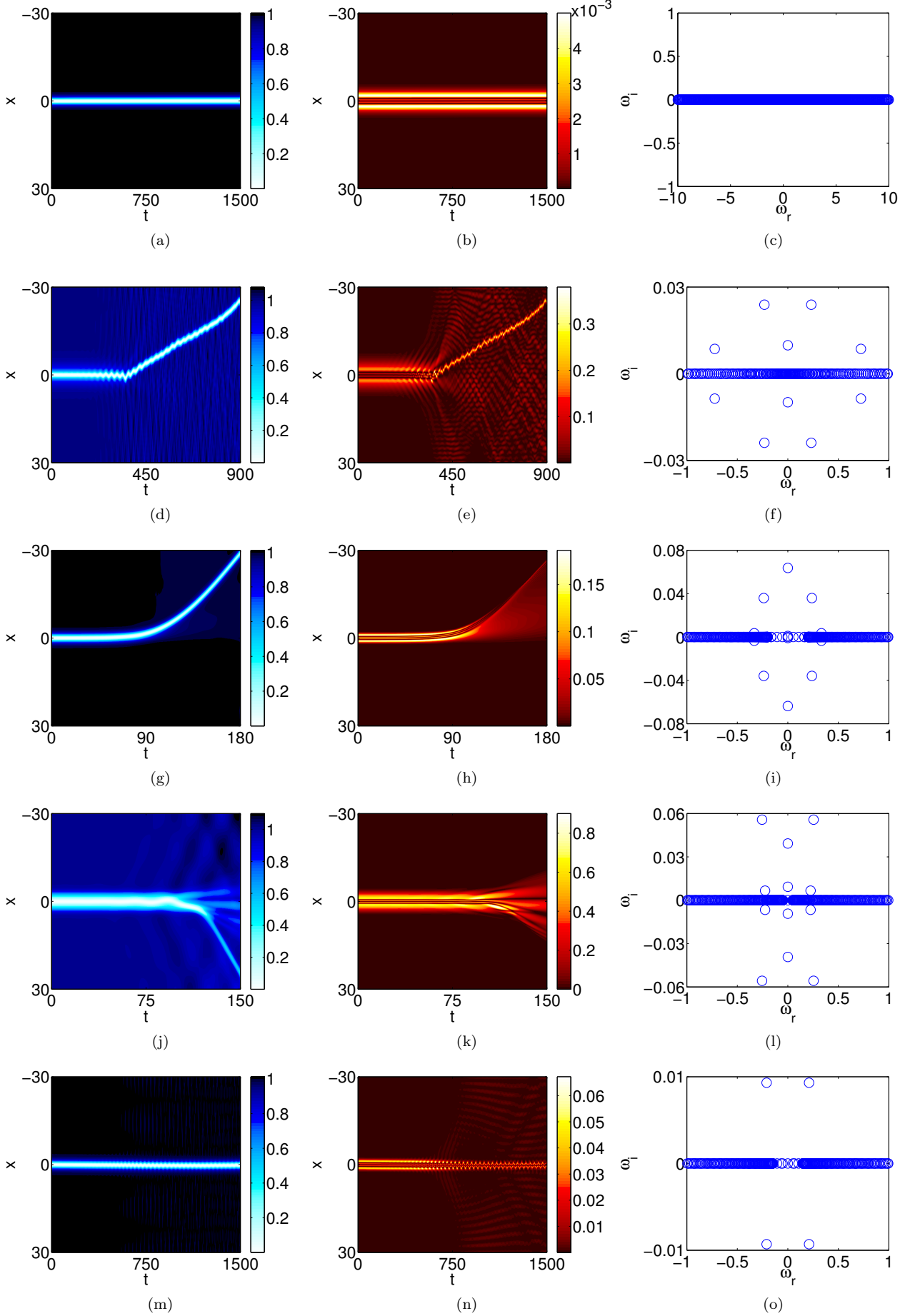


FIG. 9: (Color online) Same as in Fig. 6, but for the soliton solutions of order $n = 3$. First, second and third columns are similar in Fig. 6. First and second rows correspond to values of the parameters of $D = 0.12$, although with $\mu_+ = 0.977$ (first row) and $\mu_+ = 0.99$ (second row), respectively, whereas third and fourth rows correspond to $D = 0.04$, although with $\mu_+ = 0.8$ (third row) and $\mu_+ = 0.95$ (fourth row), respectively. Finally, the fifth row corresponds to values of the parameters of $D = 0.06$ and $\mu_+ = 0.851$.

- Sengstock, Nature Phys. **4**, 496 (2008).
- [21] C. Hamner, J. J. Chang, P. Engels, M. A. Hoefer, Phys. Rev. Lett. **106**, 065302 (2011).
 - [22] S. Middelkamp, J. J. Chang, C. Hamner, R. Carretero-González, P. G. Kevrekidis, V. Achilleos, D. J. Frantzeskakis, P. Schmelcher, and P. Engels, Phys. Lett. A **375**, 642 (2011).
 - [23] D. Yan, J. J. Chang, C. Hamner, P. G. Kevrekidis, P. Engels, V. Achilleos, D. J. Frantzeskakis, R. Carretero-González, and P. Schmelcher, Phys. Rev. A **84**, 053630 (2011).
 - [24] M. A. Hoefer, J. J. Chang, C. Hamner, and P. Engels, Phys. Rev. A **84**, 041605 (2011).
 - [25] D. Yan, J. J. Chang, C. Hamner, M. A. Hoefer, P. G. Kevrekidis, P. Engels, V. Achilleos, D. J. Frantzeskakis, and J. Cuevas, J. Phys. B **45**, 115301 (2012).
 - [26] Z. Chen, M. Segev, T. H. Coskun, D. N. Christodoulides, Yu. S. Kivshar, and V. V. Afanasjev, Opt. Lett. **21**, 1821 (1996).
 - [27] E. A. Ostrovskaya, Yu. S. Kivshar, Z. Chen, and M. Segev, Opt. Lett. **24**, 327 (1999).
 - [28] Z. Chen, M. Segev, T. H. Coskun, D. N. Christodoulides and Yu. S. Kivshar, J. Opt. Soc. Am. B **14**, 3066-3077 (1997).
 - [29] V. Achilleos, D. J. Frantzeskakis, and P. G. Kevrekidis Phys. Rev. A **89**, 033636 (2014).
 - [30] J. Dalibard, F. Gerbier, G. Juzeliūnas, and P. Öhberg Rev. Mod. Phys. **83**, 1523 (2011).
 - [31] G. Pöschl, E. Teller, Z. Phys. **83**, 143 (1933).
 - [32] P. G. Kevrekidis, D. J. Frantzeskakis, B. A. Malomed, A. R. Bishop and I. G. Kevrekidis New J. Phys. **5**, 64 (2003).
 - [33] D. M. Stamper-Kurn and M. Ueda Rev. Mod. Phys. **85**, 1191 (2013).
 - [34] H. E. Nistazakis, D. J. Frantzeskakis, P. G. Kevrekidis, B. A. Malomed, and R. Carretero-González Phys. Rev. A **77**, 033612 (2008).
 - [35] K. J. H. Law, P. G. Kevrekidis, and L. S. Tuckerman, Phys. Rev. Lett. **105**, 160405 (2010); see also **106**, 199903(E) (2011).
 - [36] M. Pola, J. Stockhofe, P. Schmelcher, and P. G. Kevrekidis Phys. Rev. A **86**, 053601 (2012).
 - [37] L. D. Landau and E. M. Lifshitz, *Quantum Mechanics*.
 - [38] C. T. Kelley, *Solving Nonlinear Equations with Newton's Method* (Fundamentals of Algorithms, SIAM, Philadelphia, 2003).
 - [39] A. H. Nayfeh and B. Balachandran, *Applied Nonlinear Dynamics: Analytical, Computational and Experimental Methods* (Wiley Series in Nonlinear Science, 1995).
 - [40] E. Hairer, S. P. Nørsett and G. Wanner, *Solving ordinary differential equations I* (Springer-Verlag, Berlin, 1993).
 - [41] R. H. Goodman, J. Phys. A: Math. Theor. **44**, 425101 (2011).
 - [42] M. Johansson and Yu. S. Kivshar, Phys. Rev. Lett. **82**, 85 (1999).
 - [43] A. Álvarez, J. Cuevas, F. R. Romero and P. G. Kevrekidis, Physica D. **240**, 767, (2011).